Therapy-Induced Senescence Drives Bone Loss

Zhangting Yao[1], Bhavna Murali[1], Qihao Ren[1], Xianmin Luo[1], Douglas V. Faget[1], Tom Cole[1], Biancamaria Ricci[2], Dinesh Thotala[3], Joseph Monahan[4], Jan M. van Deursen[5], Darren Baker[5], Roberta Faccio[2,6], Julie K. Schwarz[3], and Sheila A. Stewart[1,7,8,9]

ABSTRACT

Chemotherapy is important for cancer treatment, however, toxicities limit its use. While great strides have been made to ameliorate the acute toxicities induced by chemotherapy, long-term comorbidities including bone loss remain a significant problem. Chemotherapy-driven estrogen loss is postulated to drive bone loss, but significant data suggests the existence of an estrogen-independent mechanism of bone loss. Using clinically relevant mouse models, we showed that senescence and its senescence-associated secretory phenotype (SASP) contribute to chemotherapy-induced bone loss that can be rescued by depleting senescent cells. Chemotherapy-induced SASP could be limited by targeting the p38MAPK-MK2 pathway, which resulted in preservation of bone integrity in chemotherapy-treated mice. These results transform our understanding of chemotherapy-induced bone loss by identifying senescent cells as major drivers of bone loss and the p38MAPK–MK2 axis as a putative therapeutic target that can preserve bone and improve a cancer survivor's quality of life.

Significance: Senescence drives chemotherapy-induced bone loss that is rescued by p38MAPK or MK2 inhibitors. These findings may lead to treatments for therapy-induced bone loss, significantly increasing quality of life for cancer survivors.

Introduction

Chemotherapy is commonly administered as adjuvant therapy in patients with breast cancer to reduce the risk of recurrence after surgical resection (1, 2). Although efficacious at prolonging disease-free survival (3, 4), chemotherapy has debilitating side effects including bone loss (5) that can exceed 7% per year in women with breast cancer, which is significantly more than the 1%–2% observed in postmenopausal women. Chemotherapy can induce 4%–5% bone loss in men with prostate cancer as well (6).

Estrogen is a key anabolic agent in the bone and its loss disrupts bone homeostasis. This is best illustrated in postmenopausal women, where low estrogen contributes to 1%–2% bone loss per year and in many cases the subsequent onset of osteoporosis (7–9) that cost the U.S. health care system over 20 billion dollars in 2008 (10). Thus, bone loss has a substantial impact on a cancer survivor's quality of life and on the cost to the health care industry. Estrogen's role in bone homeostasis is complex. Indeed, estrogen exerts proosteoblastic and antiosteoclastic actions on the bone (9, 11) and regulates T-cell–induced inflammation and bone loss (12).

While estrogen's role in bone homeostasis is well established, the degree to which its loss contributes to chemotherapy-induced bone loss remains controversial (6, 13–16). Furthermore, it is unclear what other mechanisms contribute to bone loss following chemotherapy. Some clinical studies suggest that chemotherapy only induces bone loss in premenopausal women who experience amenorrhea, whereas patients that retain ovarian function display negligible changes in their bones (17). Other studies reported that adjuvant chemotherapy induces substantial bone loss in postmenopausal patients in the absence of additional estrogen loss (15). Furthermore, in many instances chemotherapy-induced bone loss is more rapid and aggressive than menopausal bone loss, and more aggressive than that observed in patients subject to complete hormone deprivation through treatment with aromatase inhibitors (6). Together, these findings suggest that chemotherapy has a direct effect on bone that results in bone loss and is independent of estrogen levels.

Materials and Methods

Mice

All mice were obtained from JAX laboratories and were housed in accordance with Washington University in St. Louis Animals Studies Committee. All animal procedures were approved by Washington University's Institutional Animal Care and Use Committees. Wild-type, 6- and 16-week-old female FVB/NJ or C57BL/6 mice were used in experiments as indicated in figure legends, unless otherwise noted. The INK-ATTAC-transgenic mice were obtained from Mayo Clinic (a kind gift from D. Baker and J.M. van Deursen).

INK-ATTAC mouse genotyping was carried out as follows: genomic DNA was extracted from mouse tissue using the RED Extract N Amp Kit (XNAT, Sigma). Primer sequences used to determine the presence of the INK-ATTAC transgene were as follows: 5′-GCAAGGTCTGTTGAATGTCGTGAAGGAAGC-3′ (forward) and 5′-CGACTAAACACATGTAAAGCATGTGCACCG-3′ (reverse). To amplify DNA of interest, 1 μL DNA extract was combined with 9 μL of master mix (XNAT kit with 0.5 μmol/L appropriate forward and

[1]Department of Cell Biology and Physiology, Washington University School of Medicine, St. Louis, Missouri. [2]Department of Orthopaedics, Washington University School of Medicine, St. Louis, Missouri. [3]Department of Radiation Oncology, Washington University School of Medicine, St. Louis, Missouri. [4]Aclaris Therapeutics, Inc., St. Louis, Missouri. [5]Department of Biochemistry and Molecular Biology and Pediatric and Adolescent Medicine, Mayo Clinic, Rochester, Minnesota. [6]Shriners Hospital for Children, St. Louis, Missouri. [7]Department of Medicine, Washington University School of Medicine, St. Louis, Missouri. [8]Siteman Cancer Center, Washington University School of Medicine, St. Louis, Missouri. [9]ICCE Institute, Washington University School of Medicine, St. Louis, Missouri.

Note: Supplementary data for this article are available at Cancer Research Online (http://cancerres.aacrjournals.org/).

Z. Yao and B. Murali contributed equally to this article.

Corresponding Author: Sheila A. Stewart, Washington University in St. Louis School of Medicine, BJC-IH ICCE Institute (Rm 7610), 660 South Euclid, Box 8228, St. Louis, MO 63110-1093. Phone: 314-362-7449; Fax: 314-362-0152; E-mail: sheila.stewart@wustl.edu

Cancer Res 2020;80:1171–82

doi: 10.1158/0008-5472.CAN-19-2348

reverse primers) in PCR tubes and amplified for one cycle at 94°C for 1 minute followed by 35 cycles at (94°C for 60 seconds, 63°C for 90 seconds, and 72°C for 2.30 seconds) and then one cycle at 72°C for 5 minutes followed by a 4°C hold. PCR products were resolved on a 2% agarose/TAE (Thermo Fisher Scientific) gel at 100 volts for 45 minutes, and visualized with UV light.

MicroCT analysis

Femurs were isolated from euthanized mice and fixed with formalin overnight. The bones were washed in PBS and placed in 70% ethanol. The femurs were then suspended in 2% agarose and scanned using microCT [μCT40 or vivaCT (Scanco Medical)] at 70 kVp, 114 μA, and 20 μm resolution. For the trabecular compartment, contours were traced on the inside of the cortical shell using 2D images of the femoral metaphysis. The end of the growth plate region was used as a landmark to establish a consistent location for starting analysis, and the next 30 slices were analyzed. The following trabecular parameters are reported for all μCT experiments: bone volume over total volume (BV/TV), trabecular thickness (Tb.Th), trabecular number (Tb.N), trabecular separation (Tb.Sp), and volumetric bone mineral density (vBMD). For the cortical compartment, contours were traced on the outside of the cortical shell using 2D images of the femoral mid-diaphysis and 100 slices were analyzed (as noted in figure legends). 3D reconstructions were generated using OsiriX, of 0.9 mm thick sections of femur right below the growth plate.

VivaCT analysis

Mice were anesthetized with isofluorane and trabecular volume in the distal femoral metaphysis of the right leg was measured using *in vivo* μCT (vivaCT 40). For the trabecular compartment, contours were traced on the inside of the cortical shell using 2D images of the femoral metaphysis. The end of the growth plate region was used as a landmark to establish a consistent location for starting analysis, and the next 30 slices were analyzed. The following trabecular parameters are reported for all μCT experiments: BV/TV, Tb.Th, Tb.N, Tb.Sp, and vBMD.

Chemotherapy administration

Doxorubicin (PHR1789, Sigma) was prepared in water and administered at 5 mg/kg via intraperitoneal injections for 4 weeks, once weekly. Mice in the vehicle group were given water. Paclitaxel (Fresenius Kabi) was purchased in suspension, each milliliter containing 6 mg paclitaxel, USP; 527 mg polyoxyl 35 castor oil NF; and 49.7% (v/v) dehydrated alcohol, USP. We prepared a 1:3 dilution in PBS and administered it via retroorbital injections for 6 weeks, once weekly.

AP20187 administration

The vehicle and AP20187 (batch no.: A113-20, Chemveda Life Sciences) were prepared with 100% ethanol: polyethylene glycol 400: 2% Tween-20 in molecular water at 4:10:86. INK-ATTAC transgenic mice were administered 2 mg/kg vehicle or AP20187 through intraperitoneal injections twice weekly for 4 weeks.

Ovariectomy

Bilateral ovariectomy was performed on mice anesthetized using isofluorane. Mice were either 6-week-old or 16-week-old at the time of the surgery, depending upon the experiment (indicated in the figure legends). The ovary was approached by a single skin incision (~5 cm) made in the "waist" region of the mouse's flank in the dorsal–ventral direction. The ovary was gently pulled through the muscle opening, a hemostat was clamped at the boundary between the ovary and uterus, and a single cut was made to detach the ovary from the uterus. A cauterizer was used to stabilize any bleeders. The muscle layer was closed with absorbable 4.0 vicryl sutures. The skin was closed with sterile sutures or wound clips and betadine applied to the incision area to avoid infection. The same procedure was repeated on the other side of the mouse. Sham-operated mice had similar incisions to the skin and peritoneum on each side, but the ovaries were not removed. To minimize discomfort post-surgery, 0.1 mg/kg buprenorphine was administered subcutaneously.

Bone histomorphology and tartrate-resistant acidic phosphatase staining

Mouse femur bones were isolated and fixed in 10% neutral buffered formalin for 24 hours. Bones were decalcified in 14% EDTA for 14 days at 4°C, embedded in paraffin, and sectioned at the histology core of the Washington University Musculoskeletal Research Center. Standard hematoxylin and eosin and tartrate-resistant acidic phosphatase (TRAP) staining techniques were used for all bone sections. Images were collected using the Zeiss Axio Scan Z1 Brightfield slide scanner, Washington University Center for Cellular Imaging (WUCCI). To quantitate the TRAP-positive cells and determine how much of their surface area covered the bone, we used the BioQuant software to quantitate osteoclasts per bone surface (Oc.S/BS and N.Oc/BS). We carried out these measurements by defining a region of interest with the stamp tool window. We then chose a diagonal line type and set the distance to the growth plate and measured the Oc.S/BS and N.Oc/BS.

Double bone labeling

Calcein (10 mg/kg, Sigma) and alizarin red (30 mg/kg, Sigma) were intraperitoneally injected into mice 9 and 2 days prior to sacrifice, respectively. Dissected long bones were fixed with 10% formalin overnight, then embedded in methymethacrylate for sectioning. Sections were left unstained and images were collected using the Zeiss Axio Scan Z1 Fluorescence slide scanner, WUCCI. Histomorphometric analysis was performed using BioQuant OSTEO 2010 software (BioQuant Image Analysis Corporation) and standard parameters to quantify mineralizing surfaces (mineral apposition rate, MAR) and bone formation rate per bone surface (BFR/BS) were performed.

RT-PCR analysis

Bones were isolated from sacrificed mice, and the marrow cavity was flushed out by centrifuging at 10,000 rpm for 10 seconds at 4°C. Bones devoid of marrow were lysed and homogenized in TRIzol (Life Technologies) containing RINO BulletBlender Navy Bead Lysis tubes (MidSci) and pulverized using a Bullet Blender Homogenizer at 4°C at speed 10 for 5 minutes. Once the bones were completely crushed, the tubes were centrifuged at 10,000 rpm for 10 minutes. The supernatant was transferred to a new tube and RNA was isolated using the RiboPure RNA Purification Kit (AM1924, Thermo Fisher Scientific). cDNA was synthesized from RNA (1 μg) using the High Capacity cDNA Reverse Transcription Kit (Applied Biosystems). Real-time PCR was performed using the TaqMan PrimeTime Gene Expression Master Mix kit and gene-specific primers and probes. All reactions were performed in duplicate. *P16* and *Il6* relative mRNA levels were calculated by the comparative cycle threshold (C_t) method [$2^{(\text{reference } C_t\text{-gene of interest } C_t)}$] using GAPDH as an internal control. The rest of the genes' mRNA were normalized to the mean of five housekeeping genes (*Hprt, Tbp, Cyclophilin, Tubulin*, and *Actin*). Primers included: *Il6*: (Forward) 5′-AGC CAG AGT CCT TCA GAG A-3′, (Reverse) 5′-TCC TTA GCC ACT CCT TCT GT-3′. *p16*:

(Forward) 5′-AAC TCT TTC GGT CGT ACC CC-3′, (Reverse) 5′-TCC TCG CAG TTC GAA TCT G-3′. *Ccl3*: (Forward) 5′-CGATGAATTGGCGTGGAATC-3′, (Reverse) 5′-CCTTGCTGTTCTTCTCTGTACC-3′. *Mcsf*: (Forward) 5′-GGAAGATGGTAGGAGAGGGTA-3′, (Reverse) 5′-AGGATGAGGACAGACAGGT-3′. *Mmp12*: (Forward) 5′-GCTCCTGCCTCACATCATAC-3′, (Reverse) 5′- GGCTTCTCTGCATCTGTGAA-3′. *Hmgb1*: (Forward) 5′-AATGGCGGTTAA AGGAGAGTC-3′, (Reverse) 5′-TGGCAAAGCAAGGAGTGAT-3′. *Igfbp4*: (Forward) 5′-GAT CCA CAC ACC AGC ACT T-3′, (Reverse) 5′-CTC TTC ATC ATC CCC ATT CCA-3′. *Cxcl2*: (Forward) 5′-CTT TCC AGG TCA GTT AGC CTT-3′, (Reverse) 5′-CAG AAG TCA TAG CCA CTC TCA AG-3′. *Gapdh*: (Forward) 5′-AATGGTGAAGGTCGGTGTG-3′, (Reverse) 5′-GTGGAGTCATACTGGAACATGTAG-3′. *Hprt*: (Forward) 5′-GTTGTTGGATATGCCCTTGAC-3′, (Reverse) 5′-TCAACAGGACTCCTCGTATT-3′. *Tbp*: (Forward) 5′-CCCTTCACCAATGACTCCTATG-3′, (Reverse) 5′-CAGCCAAGATTCACGGTAGAT-3′. *Cyclophilin*: (Forward) 5′-TTCACCTTCCCAAAGACCAC-3′, (Reverse) 5′-CAAACACAAACGGTTCCCAG-3′. *Tubulin*: (Forward) 5′-TCTTGTCACTTGGCATCTGG-3′, (Reverse) 5′-CGCGAAGCAGCAACCAT-3′. *Actin*: (Forward) 5′-TTTCCAGCCTTCCTTCTTGG-3′, (Reverse) 5′-GGCATAGAGGTCTTTACGGATG-3′. *Ptprc*: (Forward) 5′- TTT CCA ATG TGC TGT GTC CT-3′, (Reverse) 5′- TGA AGA AGA GAG ATC CAC CCA-3′. *Col1a1*: (Forward) 5′- CAT TGT GTA TGC AGC TGA CTT C-3′, (Reverse) 5′- CGC AAA GAG TCT ACA TGT CTA GG-3′. *Col2a1*: (Forward) 5′- AGC CTT CTC GTC ATA CCC T-3′, (Reverse) 5′- GCA GAG ATG GAG AAC CTG GTA-3′. *Pecam*: (Forward) 5′-TGT TGG AGT TCA GAA GTG GAG-3′, (Reverse) 5′- TCA TTG GAG TGG TCA TCG C-3′. *Fabp4*: (Forward) 5′-CCT TTC ATA ACA CAT TCC ACC AC-3′, (Reverse) 5′- AAA TCA CCG CAG ACG ACA G-3′. *p21*: (Forward) 5′-GAA GAG ACA ACG GCA CAC T-3′, (Reverse) 5′-CAG ATC CAC AGC GAT ATC CAG-3′.

Cell isolation and sorting from murine bones

Bones (femurs and tibias) were harvested from euthanized mice and placed in cold DMEM/F12 (Gibco). Muscle and connective tissues were removed. Bones were gently ground and then cut into small fragments. Fragments were transferred and digested with fresh 2 mg/mL collagenase (Sigma, C0130) in DMEM/F12 on a rotating water bath at 37°C for 30 minutes. Following the first digestion, the released cell suspension was filtered through a 70-μm nylon mesh into a collection tube and placed on ice. A second digestion of the remaining fragments was performed and the cell suspension was filtered into the same collection tube. Reactions were quenched with FACS buffer (PBS plus 0.5% BSA) with 2 mmol/L EDTA. Following FACS buffer wash and RBC lysis, dissociated cells were labeled with anti- CD45 magnet microbeads (Miltenyi Biotec) and enriched into a $CD45^+$ fraction (hematopoietic cells) and $CD45^-$ fraction (bone stromal cells) by magnetic-activated cell sorting (MACS, Miltenyi Biotec). Cells were stained with fluorochrome antibodies for 20 minutes on ice for cell sorting. We used CD45 (BioLegend, 103126), CD11b (BD Biosciences, 557397), CD3e (BD Biosciences, 553062), CD19 (eBioscience, 17-0193-80), Sca-l (Ly6A/E) (BD Biosciences, 563288), and c-kit (BioLegend, 105813) to isolate independent populations from the $CD45^+$ fraction and CD45 (BD Biosciences, 553080) and CD31 (eBioscience, 48-0311-80) for cells from the $CD45^-$ fraction. Using a BD FACSAria III Cell Sorter (BD Biosciences), indicated cell populations were directly sorted into 650 μL RLT containing 2-β mercaptoethanol lysis buffer and processed for RNA extraction with RNeasy Micro Kit (Qiagen). cDNA was synthesized using the High Capacity cDNA Reverse Transcription Kit (Applied Biosystems). RT-PCR was used to validate the cell populations and test the senescence signatures. Primers used are listed in RT-PCR section.

Single-limb irradiation

Mice were anesthetized with 2% isoflurane prior to irradiation to the right leg by shielding the rest of the body with lead. The mice were irradiated with a single dose of 20 Gy using an RS-2000 (Rad Source) irradiator at a dose rate of 1.81 Gy/minute at 160 kVp X-rays.

Senescence-associated β-galactosidase staining

Senescence-associated β-galactosidase (SA-β-Gal) staining in femurs of mice was performed on frozen sections that were fixed in 0.2% glutaraldehyde for 10 minutes at 4°C. Slides were washed in PBS and then submerged in X-gal solution (1 mg/mL 5-bromo-4-chloro-3-indolyl β-D-galactopyranoside, 150 mmol/L NaCl, 2 mmol/L $MgCl_2$, 5 mmol/L $K_3Fe(CN)_6$, 5 mmol/L $K_4Fe(CN)_6$, 40 mmol/L NaPi pH 6.0, in H_2O). The X-gal solution was passed through a 0.45-μm filter before use to remove particulate. Slides were kept at 37°C in the dark until the stain developed (~6 hours). After staining, the slides were fixed for 10 minutes in 0.2% glutaraldehyde at room temperature, washed in PBS, and then the nuclei were counterstained using Nuclear Fast Red (Sigma).

SA-β-Gal staining on fresh visceral fat was performed after fixation in 4% paraformaldehyde (PFA) at 4°C for 20 minutes. Fat tissues were then immersed in X-gal solution and kept at 37°C in the dark for approximately 6 hours. After staining, fat tissues were fixed in 4% PFA, washed with PBS, and images acquired.

MK2 IHC

Neutral buffered formalin-fixed, paraffin embedded mouse bones that had been decalcified in 14% EDTA for 14 days were cut in serial sections (5 μm). IHC staining was performed on a BOND RXm Fully Automated Research Stainer from Leica Biosystems. Phosphorylated-MK2 was stained using the Bond Polymer Refine Detection Kit (catalog no: DS9800) according to the manufacturer's recommendations for rabbit primary antibodies. In brief, tissue sections were baked for 15 minutes at 60°C, dewaxed, then heat-induced epitope retrieval was performed with ER2 (EDTA) for 20 minutes at 100°C followed by 5 minutes of blocking of endogenous peroxidase activity, primary antibody phosph-MK2 (Cell Signaling Technology, 1:100; catalog no. 3041S) was incubated for 1 hour at room temperature. A no primary negative control was simultaneously stained. Next, slides were subject to Bond washes and then incubated with the polymer anti-rabbit Poly-HRP-IgG for 8 minutes. Finally, DAB was applied and counterstaining was done with hematoxylin. Tissue was then dehydrated in ethanol followed by xylene, and slides were mounted with xylene-based mounting media. For quantification, whole-tissue slide scans were obtained using a Zeiss Axio Scan Z1 Brightfield slide scanner. Images were analyzed with HALO software and the whole tissues were defined as regions of interest (ROI). We adjusted and detected the threshold of positive p-MK2 staining on a single nuclear basis to quantify the percentage of positive cells in a given ROI.

Oral dosage of p38MAPK and MK2 inhibitors

The p38MAPK small-molecule inhibitor CDD111 (p38i) (Aclaris Therapeutics, Inc.) was compounded as described previously (18). The p38MAPK/MK2 small-molecule pathway inhibitor ATI-450 (MK2Pi) was compounded at 1,000 ppm (Aclaris Therapeutics, Inc.). Female C57BL/6 mice were fed *ad libitum*. Mice were randomized onto inhibitor containing or regular chow on the same day as their first doxorubicin dose.

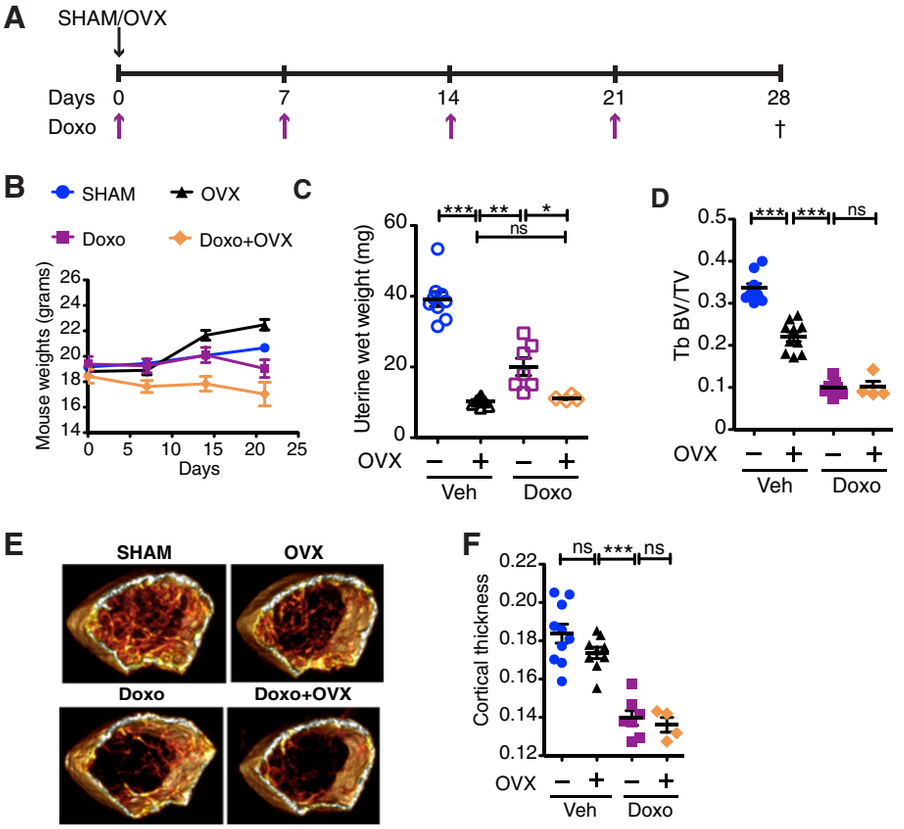

Figure 1.

Chemotherapy-induced bone loss is more severe than estrogen-dependent bone loss. **A,** Schematic of the experimental timeline for OVX surgery and dosing regimen for doxorubicin (Doxo; 5 mg/kg) in 6-week-old FVB/NJ mice. Dagger, time of sacrifice. **B,** Mouse weights for the duration of the experiment on indicated days. **C,** Uterine wet weights, measured as a surrogate for estrogen levels in SHAM or OVX mice treated with vehicle (Veh) or doxorubicin. **D,** Trabecular (Tb) volume (TV) compared with bone volume (BV) of femurs, presented as Tb BV/TV. **E,** Representative 3D reconstructions for each of the treatment groups. **F,** Cortical thickness of treated bones. $N \geq 4$ mice per group. All data are presented as mean ± SEM. *, $P \leq 0.05$; **, $P \leq 0.01$; ***, $P \leq 0.001$; ns, not significant. Comparisons are indicated by capped lines.

Statistical analysis

All statistical analyses were carried out using GraphPad Prism. Numerical data are expressed as mean ± SEM. All qRT-PCR data are presented as mean ± SD. Between-group comparisons of mouse results were performed by Student *t* test or one-way ANOVA.

Results

Chemotherapy is a potent inducer of DNA damage (19–22) that can robustly induce cellular senescence (21–24). Recent work demonstrated that senescence drives age-related bone loss (25), raising the possibility that it contributes to chemotherapy-induced bone loss. To study the role of senescence in chemotherapy-induced bone loss, we established a clinically meaningful mouse model by employing doxorubicin (DOXO), an anthracycline-based chemotherapeutic agent that is widely used to treat patients with early and advanced breast cancer (26, 27), and results in adverse effects on bone in adults (28) and children alike (29). Having established this model, we compared it with a bone loss model that is completely dependent on estrogen, namely ovariectomy (OVX), which induces robust bone loss in the absence of senescence (30).

First, we compared the effects of chemotherapy versus OVX-induced bone loss in a cohort of 6-week-old, wild-type, female FVB/NJ mice. Subsets of the cohort were subjected to OVX or SHAM surgery, followed by once weekly treatments of vehicle or a biologically relevant dose of doxorubicin (5 mg/kg; refs. 31, 32) for 4 consecutive weeks (**Fig. 1A**). As expected, OVX mice gained weight throughout the time course, while doxorubicin-treated mice lost only a negligible amount of weight that did not correlate with bone loss (**Fig. 1B**). At endpoint, we assessed estrogen levels in mice by measuring uterine weight, which is used as a surrogate of biologically active estrogen levels (33). Mice undergoing OVX experienced a 73.76% loss in uterine weight compared with SHAM mice (**Fig. 1C**), while doxorubicin-treated mice lost 48.91%. When OVX and doxorubicin treatments were combined, the uterine weights were identical to uteri from OVX-treated mice demonstrating that OVX led to the lowest levels of estrogen.

We next used μCT to measure trabecular and cortical bone volumes in the femurs of mice in each experimental group. μCT analysis on the femoral metaphysis and mid-diaphysis of doxorubicin-treated mice revealed a significant decrease in trabecular bone volume (−70.41%) compared with vehicle-treated SHAM mice, as measured by the ratio of BV/TV (**Fig. 1D**) and corroborated by 3D reconstructions (**Fig. 1E**). Doxorubicin treatment decreased all bone parameters including trabecular bone thickness (Supplementary Fig. S1A), vBMD (Supplementary Fig. S1B), and trabecular bone number while increasing the separation between the trabecular bones (Supplementary Fig. S1C and S1D). In addition, the cortical thickness was decreased by 23.98% in the doxorubicin group compared with vehicle-treated SHAM mice (**Fig. 1F**).

Next, we compared the impact of doxorubicin versus estrogen deficiency alone on bone density. As expected, μCT analysis of the femoral metaphysis showed a reduction in trabecular bone volume in OVX mice (black symbols, −34.35%) relative to the SHAM group (blue symbols; **Fig. 1D**). However, doxorubicin-treated mice (purple symbols) showed a more striking decrease in trabecular bone volume relative to the OVX control group (black symbols), indicating that doxorubicin treatment induced bone loss beyond the impact of

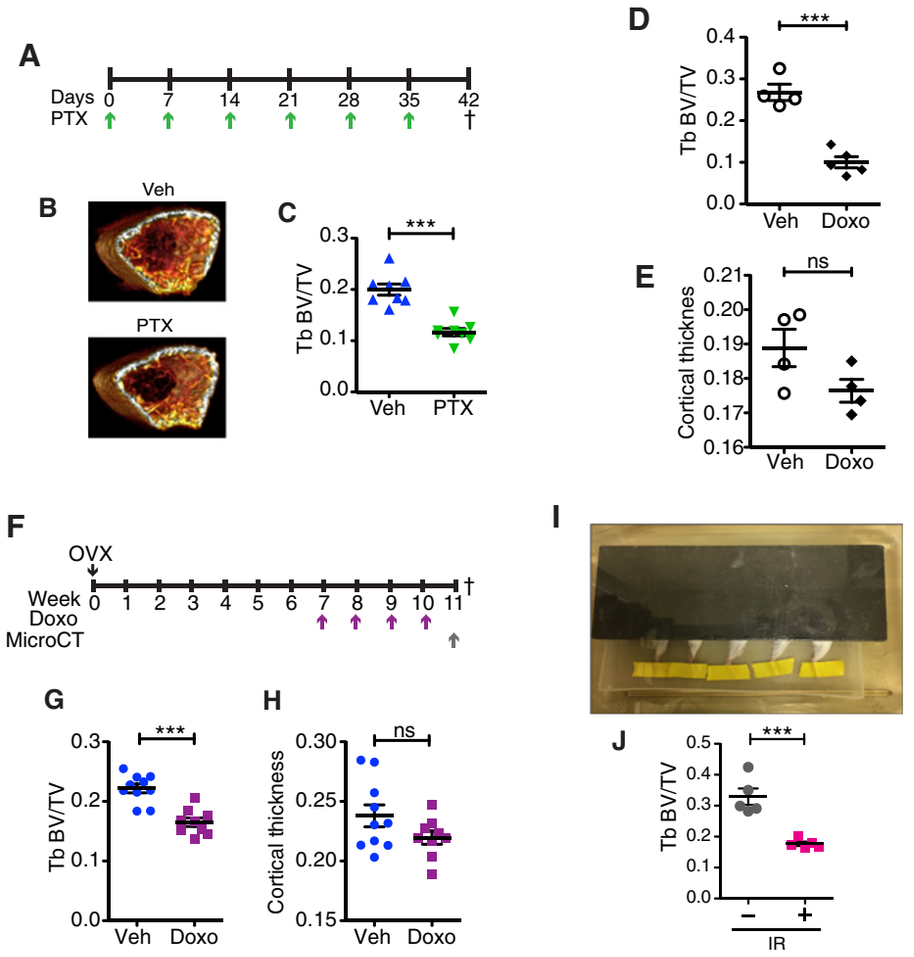

Figure 2.

Chemotherapy can induce bone loss independent of estrogen loss. **A,** Schematic of experimental setup and dosing regimen for paclitaxel (PTX; 10 mg/kg) in 6-week-old C57BL/6 female mice. Dagger, time of sacrifice. **B,** Representative 3D reconstructions, generated using OsiriX, of 0.9-mm thick sections of femur right below the growth plate for each of the treatment groups. **C,** Trabecular bone parameter of femurs after μCT presented as trabecular (Tb) bone volume (BV) to trabecular volume (Tb BV/TV). $N = 8$ per group. **D** and **E,** Tb BV/TV in 6-week-old C57BL/6 male mice treated with four once weekly doses of doxorubicin (Doxo, 5 mg/mL) or vehicle (Veh; **D**) and cortical thickness in the same male mice (**E**). $N \geq 4$ per group. **F,** Schematic of experimental timeline showing dosing regimen for doxorubicin (5 mg/kg) after stabilization of OVX-induced bone loss. Dagger, time of sacrifice. **G** and **H,** Trabecular volume (TV) compared with bone volume of femurs, presented as Tb BV/TV (**G**), and cortical thickness of femurs at 11 weeks post-OVX in mice treated with vehicle (Veh) or doxorubicin (**H**). $N \geq 9$ per group. **I,** Picture of single-limb irradiation setup with only the right leg exposed and the rest of the body covered by a lead shield. The right hind legs of 6-week-old FVB/NJ mice received 20 Gy radiation and 4 weeks later the irradiated (IR) and contralateral femurs were isolated and scanned using μCT. **J,** Trabecular volume compared with bone volume of femurs, presented as Tb BV/TV for the irradiated leg (+) and contralateral control (−). $N = 5$ per group. All data are presented as mean ± SEM. ***, $P \leq 0.001$; ns, not significant.

estrogen loss alone. A similar pattern of decrease in cortical bone volume was observed in OVX (−5.48%) and doxorubicin-treated mice (−23.98%), relative to the SHAM mice, respectively (**Fig. 1F**). Remarkably, even though the uterine weights (indicative of estrogen levels) of OVX mice were significantly lower than doxorubicin-treated mice (**Fig. 1C**), the latter group experienced far more bone loss. If estrogen deficiency were the sole perpetrator of bone loss following chemotherapy, we would expect to see the same degree of bone loss in OVX and doxorubicin-treated mice. These data suggest that chemotherapy-induced bone loss is due, at least in part, to an estrogen-independent mechanism.

To exclude strain-dependent effects, we performed the identical experiment in 6-week-old C57BL/6 mice and observed similar trabecular bone loss following chemotherapy (Supplementary Fig. S1E). Similar results were obtained when C57BL/6 mice were treated with a second commonly used chemotherapeutic agent, paclitaxel (**Fig. 2A**). μCT analysis of the trabecular bone volume showed a striking decrease (−41.6%) in paclitaxel-treated mice relative to age-matched controls (**Fig. 2B** and **C**) with associated changes in trabecular number, separation, thickness, and vBMD (Supplementary Fig. S2A–S2D). Paclitaxel treatment was also associated with a reduction in uterine weight (Supplementary Fig. S2E). Finally, because estrogen is a chief regulator of bone metabolism in both males and females (7, 34–38), we treated male mice with 4 weekly doses of doxorubicin (5 mg/kg). Chemotherapy induced a significant decrease (−62.59%) in trabecular bone volume (**Fig. 2D**) and a decrease (−6.59%) in cortical bone

volume (**Fig. 2E**) in doxorubicin-treated male mice relative to vehicle-treated mice, similar to the changes observed in female mice.

To create a clinically relevant scenario of postmenopausal chemotherapy treatment where estrogen levels are already low, we performed OVX in 6-week-old FVB/NJ mice, and then measured bone mass (measured as BV/TV) longitudinally in the same mice at 4 and 6 weeks post-OVX by *in vivo* imaging (VivaCT; Supplementary Fig. S3A). We found that bone loss ceased by 4 weeks post-OVX and the same BV/TV was maintained at 6 weeks (Supplementary Fig. S3B). To determine whether chemotherapy induced additional bone loss in the postmenopausal scenario, 7 weeks post-OVX, mice were treated with vehicle or doxorubicin once weekly for 4 weeks (**Fig. 2F**). At the end of chemotherapy treatment, bone volume changes were evaluated via a single μCT scan. As observed in postmenopausal women treated with chemotherapy, doxorubicin-treated mice lost more trabecular bone volume relative to vehicle-treated mice over the 4-week period after OVX-induced bone loss (**Fig. 2G**). The mice also lost cortical bone (**Fig. 2H**). This demonstrates that chemotherapy induces bone loss in a low-estrogen setting and establishes the clinical relevance of our model.

To ask whether bone loss could be induced in an estrogen-sufficient setting, we turned to radiation, which induces marked bone loss in humans and mice (39–41). To avoid the ovaries, we used single-limb irradiation and shielded the remainder of the animal (**Fig. 2I**). We selectively irradiated the right hind limb of 6-week-old female FVB/NJ mice with a single dose of 20 Gy (40, 41). Uterine weights were measured at endpoint to ensure that the radiation had no impact on estrogen levels. The uterine weights from irradiated mice were stable and comparable with untreated, wild-type 10-week-old female FVB/NJ mice (Supplementary Fig. S4A). μCT analysis of the femurs revealed a significant decrease in trabecular bone volume (−46.28%) in the radiated limbs compared with the contralateral control limbs (**Fig. 2J**). As expected, other measures of bone loss including changes in trabecular vBMD, trabecular thickness and number, and increased separation of trabecular bone, were also observed only in the irradiated femurs (Supplementary Fig. S4B–S4F).

Both chemotherapy and radiation can induce robust senescence, and recent work demonstrated that age-related increases in senescent cells drive bone loss (25). Thus, we hypothesized that senescence contributes to chemotherapy- and radiation-induced bone loss. To assess the presence of senescent cells in bone resident cells, we isolated the irradiated and contralateral tibias from mice subjected to 20 Gy single-limb radiation, flushed the bone marrow, and extracted RNA from bone resident cells and performed qRT-PCR. To assess for senescence-related alterations we assayed for changes in the senescence markers *p16INK4a* (*p16*) and *Hmgb1* and senescence-associated secretory phenotype (SASP) factors. Upon qRT-PCR analysis, we observed a 3.4-fold increase in *p16* levels and a 0.71-fold drop in *Hmgb1* in the irradiated tibias relative to the nonirradiated contralateral tibias (**Fig. 3**). These changes correlated with increased SASP expression including *Il6* (1.4-fold), *Ccl3* (1.6-fold), *Mcsf* (2.0-fold), and *Mmp12* (2.2-fold; **Fig. 3**). We next asked whether there was similar activation in the bones of mice treated with chemotherapy. We isolated tibias from 6-week-old FVB/NJ mice at 48 hours or 7 days following a single dose of vehicle or doxorubicin (25 or 10 mg/kg). As above, bone marrow was removed from the tibias and RNA was extracted from bone resident cells. Similar to irradiated bones, we observed a significant upregulation of *p16* (2.46-fold) and a concordant decrease in *Hmgb1* (0.78-fold) in the bones from doxorubicin-treated mice compared with vehicle

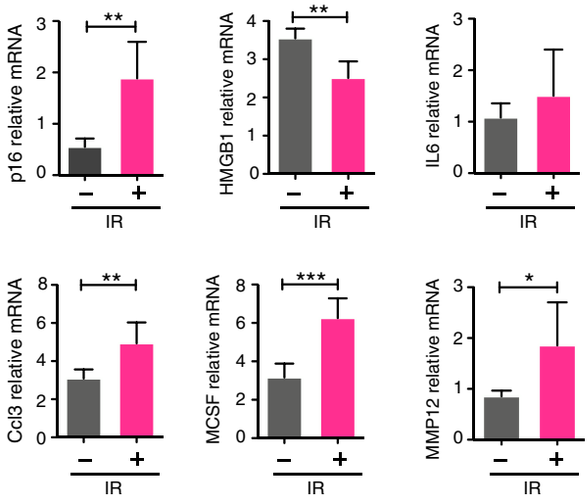

Figure 3.

Radiation induces senescence in the bone. Six-week-old FVB/NJ mice received 20 Gy radiation to the right hind limb and 48 hours later the tibias were isolated, bone marrow was removed, and tibias were crushed and used to prepare RNA from bone-residing cells. **A,** *p16, Hgmb1, Il6, Igfbp4, Cxcl2, Ccl3, Mcsf,* and *Mmp12* mRNA levels in crushed tibias (irradiated vs. contralateral) devoid of marrow, as a measure of senescence induction. $N = 5$ per group. All qRT-PCR data are presented as mean ± SD. *, $P \leq 0.05$; **, $P \leq 0.01$; ***, $P \leq 0.001$.

(**Fig. 4A**). These changes were accompanied by increases in SASP factors including *Il6* (7.5-fold), *Ccl3* (1.7-fold), *Mcsf* (1.8-fold), and *Mmp12* (2.5-fold) in the tibias from doxorubicin-treated mice (**Fig. 4A**). Importantly, we failed to observe increases in these factors in mice subject to OVX (Supplementary Fig. S5), demonstrating that estrogen loss is not sufficient to induce senescence in the bone.

To determine which cells were senescing within the bones of chemotherapy-treated mice, we isolated femurs and stained vehicle- and doxorubicin-treated bones for SA-β-Gal, a well-established marker of senescence (42–44). We found SA-β-Gal increased by approximately 40% in femurs from doxorubicin-treated mice relative to vehicle-treated mice (**Fig. 4B**). Upon histologic analysis, we found that SA-β-Gal–positive cells were present in the marrow space, as well as along the trabecular bone of chemotherapy-treated mice. To identify which cells were senescing in the bone following chemotherapy, we isolated cells by crushing whole bones and digesting them with collagenase to release bone resident cells. Following digestion, we used MACS CD45 beads to separate $CD45^+$ and $CD45^-$ cells. The $CD45^+$ fraction was further stained with antibodies against CD3e, CD19, and CD11b to isolate T cells, B cells, and myeloid cells, respectively. We also stained cells with antibodies against Sca-I and cKit to isolate hematopoietic stem cells (HSC). The $CD45^-$ fraction was further stained with anti-CD31 to separate endothelial cells from bone resident cells (gating strategy can be found in Supplementary Fig. S6A and S6B). Following cell sorting, we performed qRT-PCR to first confirm the identity of our sorted populations. As shown in Supplementary Fig. S6C, we successfully isolated populations as indicated in our flow sorting. To demonstrate the induction of senescence in the different populations, we assessed *p16, p21, Hmgb1*, and SASP expression by qRT-PCR. We found that only the $CD45^-CD31^-$ population showed a significant increase in the senescent marker *P16* (**Fig. 4C**). Consistent with the increased *P16* levels, we

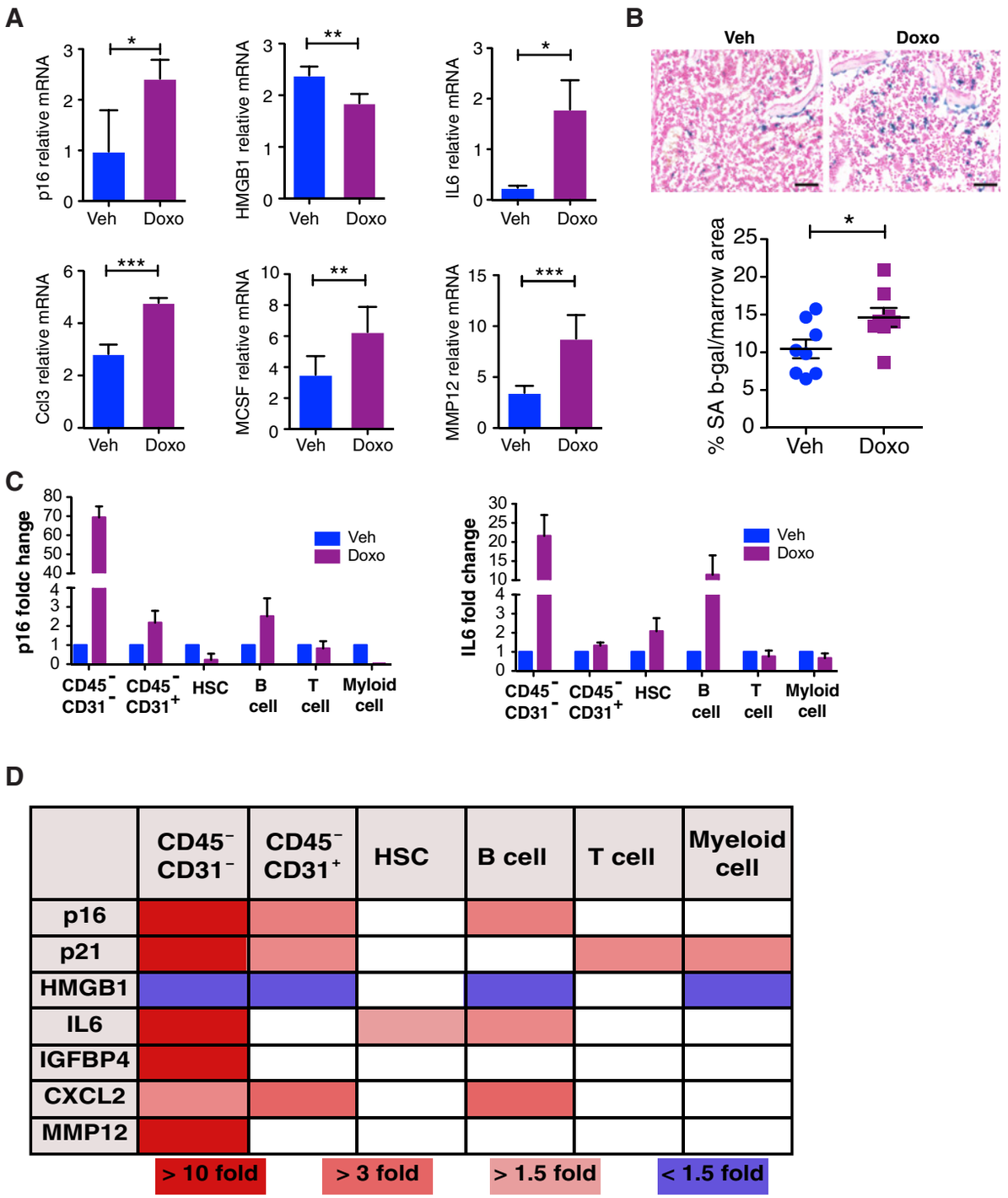

Figure 4.

Chemotherapy induces senescence in the bone. **A,** Mice were treated with vehicle (Veh) or doxorubicin (Doxo) and 48 hours later, legs were isolated, marrow was removed, and bones were crushed and used to make mRNA from bone resident cells. Expression of *p16, Il6* (6-week FVB, 25 mg/kg), and expression of *Hgmb1*, *Ccl3, Mcsf,* and *Mmp12* (16-week C57Bl/6, 10 mg/kg) mRNA levels in crushed tibias was measured by qRT-PCR. $N \geq 5$ per group. Data are presented as mean ± SD. **B,** SA-β-Gal staining in femurs isolated 7 days after a single doxorubicin dose in 6-week-old FVB/NJ mice (top). Scale bars, 100 μm. Bottom, quantification of SA-β-Gal. $N = 8$ per group. Data are presented as mean ± SEM. *, $P \leq 0.05$; **, $P \leq 0.01$; ***, $P \leq 0.001$. **C,** Six-week-old C57BL/6 mice were treated with vehicle of 25 mg/kg doxorubicin and 48 hours later, legs were dissociated and bone resident cells were isolated and stained with antibodies against CD45, CD31, cKit, Scal, and various hematopeoitic markers, followed by sorting for HSC, T cells, B cells, myeloid cells, and $CD45^{-}CD31^{+}$ and $CD45^{-}CD31^{-}$ populations. Expression of *p16* and *IL6* mRNA were quantified in the indicated populations. **D,** mRNA expression of other SASP factors were detected in the populations as indicated (graphs of expression can be found in Supplementary Fig. S7). $N = 2$. All qRT-PCR data are presented as mean ± SD.

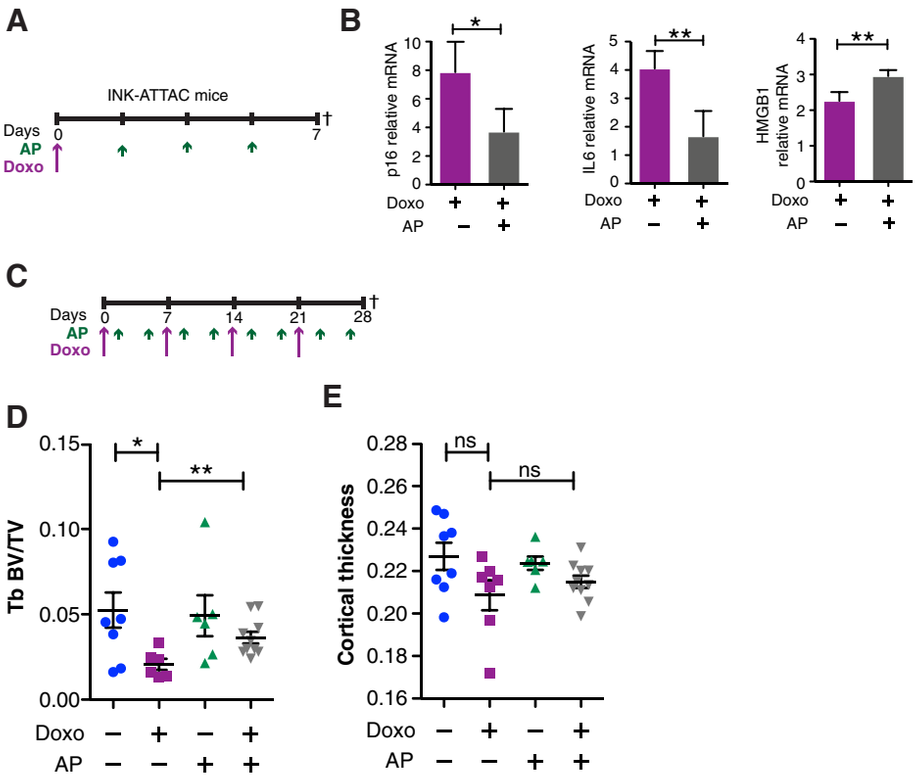

Figure 5.

Clearance of senescent cells rescues chemotherapy-induced bone loss. **A,** Experimental schematic for 1-week timepoint showing a single dose of doxorubicin (Doxo; 10 mg/kg) and three doses of AP20187 (AP; 2 mg/kg) in 16-week-old C57BL/6 INK-ATTAC mice. Dagger, time of sacrifice. **B,** qRT-PCR analysis of *p16, Il6*, and *Hgmb1* from mRNA obtained from bone resident cells present in tibias devoid of marrow from INK-ATTAC mice 7 days after dosing with doxorubicin and AP20187 (AP). $N \geq 3$ per group. qRT-PCR data are presented as mean ± SD. **C,** Experimental schematic for 4-week timepoint, with dosing frequency of doxorubicin (5 mg/kg) and AP20187 (2 mg/kg) and symbols as in **A**. **D** and **E,** Trabecular (Tb) BV/TV of femurs (**D**) and cortical thickness of femurs (**E**). $N \geq 6$ per group. Data are presented as mean ± SEM. *, $P < 0.05$; **, $P \leq 0.01$; ns, not significant.

found that the $CD45^{-}CD31^{-}$ population expressed increased levels of *p21* and decreased levels *Hmgb1* (**Fig. 4D**; Supplementary Fig. S7). Finally, the $CD45^{-}CD31^{-}$ population also expressed a significant increase in SASP factors including *Il6* (**Fig. 4C**), *Igfbp4, Cxcl2,* and *Mmp12* (**Fig. 4D**; Supplementary Fig. S7). Together this work suggests that the only population robustly induced to senesce was the bone resident cells but not $CD31^{+}$ endothelial cells or $CD45^{+}$ cells.

Having found evidence of senescence in the bones following irradiation and chemotherapy, next we asked whether senescence drove bone loss in these scenarios. To establish a model that minimized the impact of estrogen on bone loss and mitigated any effects on bone development, we subjected 16-week-old C57BL/6 mice to SHAM or OVX surgery. In agreement with earlier work (45, 46), we found that over the 4-week time course (Supplementary Fig. S8A), 16-week-old mice failed to lose bone following OVX surgery (Supplementary Fig. S8C–S8H) despite being deprived of estrogen, as evidenced by a significant reduction in uterine weight (Supplementary Fig. S8B). It should be noted that after 3 months, OVX-treated mice maintained low estrogen levels as evidenced by reduced uterine weight (Supplementary Fig. S8I) and eventually lost cortical bone but not trabecular bone (Supplementary Fig. S8J and S8K). This demonstrated that estrogen contributes to bone homeostasis as reported previously (30), just not within the 4-week time course under study. In contrast, treating 16-week-old C57BL/6 mice with four weekly doses of doxorubicin (Supplementary Fig. S8B–S8H) or subjecting these mice to single-limb irradiation (Supplementary Fig. S9A and S9B) resulted in robust bone loss in the same 4-week time course. Together, these studies establish that, unlike estrogen loss alone, chemotherapy and radiation induce bone loss within 4 weeks in a fully mature 16-week-old mice.

To establish a role for senescence in chemotherapy-induced bone loss with minimal effects of estrogen, we turned to the INK-ATTAC transgenic mouse model (47, 48). In this model, the p16INK4a minimal promoter drives expression of a conditional suicide gene that kills senescent cells upon administration of the dimerization drug AP20187 (AP). Using this model, it was shown that senescent cells drive age-related bone loss (25) while having no impact on OVX-driven bone loss (30). We postulated that if senescence mediates chemotherapy-induced bone loss, then the clearance of senescent cells would protect against this bone loss. To test our hypothesis, we treated 16-week-old female INK-ATTAC (C57BL/6) transgenic mice with vehicle or a single dose of 10 mg/kg doxorubicin. These mice were then randomized to receive vehicle or three doses of AP20187 (2 mg/kg) and sacrificed 7 days post- doxorubicin injection (**Fig. 5A**), a time at which we observed increased senescence in the bones of doxorubicin-treated wild-type animals (**Fig. 4B**). We confirmed that AP20187 could reduce doxorubicin-induced senescence in the bones of INK-ATTAC mice, as illustrated by a decrease in *p16* (0.47-fold) and *Il6* levels (0.41-fold), and a concordant increase of *Hmgb1* (1.33-fold) levels (**Fig. 5B**). Next, we extended the experimental timeline to 4 weeks, wherein the mice received four weekly doses of doxorubicin (5 mg/kg) to induce senescence and four cycles (twice weekly) of AP20187 (2 mg/kg) to kill senescent cells (**Fig. 5C**). At 4 weeks, mice were sacrificed, and we analyzed visceral fat for evidence of senescence and found, as expected, that doxorubicin treatment (purple symbols) increased SA-β-Gal, but we failed to see a rescue of senescence in fat upon AP20187 treatment (gray symbols; Supplementary Fig. S10A and S10B). Strikingly, μCT analysis of femoral metaphysis revealed that mice receiving the combination treatment (DOXO+AP, gray) had significantly higher trabecular bone volume (+75.84% increase) compared with mice receiving doxorubicin alone (purple symbols; **Fig. 5D**), and a similar

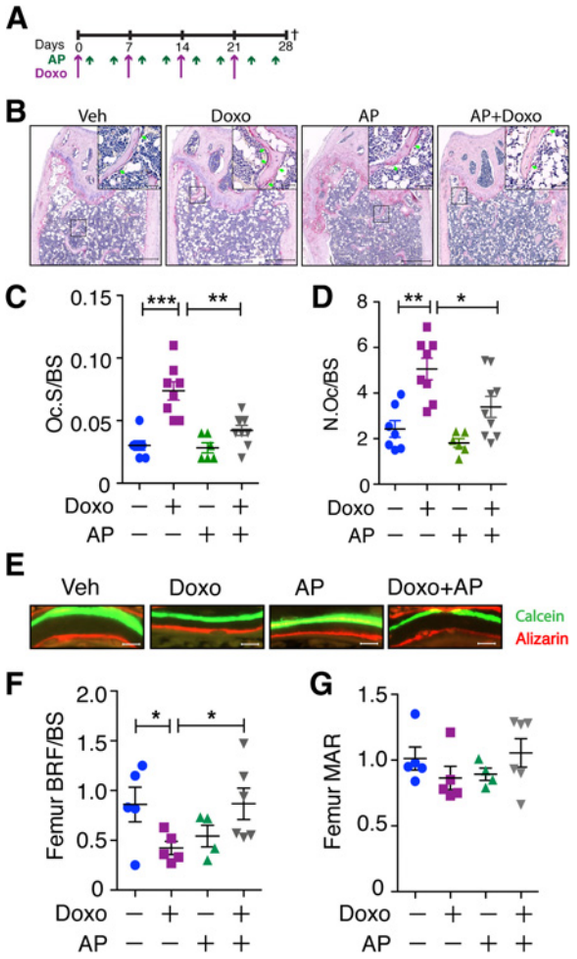

Figure 6.

Clearance of senescent cells rescues osteoblast function and reduces osteoclasts. **A,** Experimental schematic as laid out in **Fig. 5**. **B,** Representative images of TRAP staining of bones from mice treated as indicated. Scale bars, 500 μm in main images and 50 μm in insets. **C** and **D,** Histomorphometric analysis of TRAP-stained sections to quantify the ratio of osteoclast surface to bone surface [Oc.S/BS (/mm); **C**] and the number of osteoclasts per bone surface [N.Oc/BS (/mm); **D**]. **E–G,** Histomorphometric analysis of double bone labeling of femurs from mice injected with calcein (green) and alizarin (red) 7 days apart. **E,** Representative images. **F** and **G,** Quantification of bone formation rate [BFR/BS (mcm^3/mcm^2/d); **F**] and mineral apposition rate [MAR (mcm/d); **G**]. Scale bar, 10 μm. $N \geq 6$ per group. All data are presented as mean ± SEM. *, $P \leq 0.05$; **, $P \leq 0.01$; ***, $P \leq 0.001$. AP, AP20187.

trend was noted in the cortical bone (**Fig. 5E**). Thus, despite the fact that we failed to reduce senescence in the fat following doxorubicin treatment, we did rescue the bone loss in this model.

Bone homeostasis is maintained by a balanced coupling of bone formation and resorption, and investigation into age-related bone loss suggested that senescent cells within the bone led to an uncoupling of these activities (25). To ask whether a similar decoupling occurs following chemotherapy-induced senescence, we performed histomorphometric analysis on the femurs of mice treated with DOXO ± AP (**Fig. 6A**). Quantification of osteoclasts by TRAP staining (**Fig. 6B**) revealed a significant decrease in osteoclast-covered surface per bone surface (Oc.S/BS) and osteoclast number per bone surface (N.Oc/BS; **Fig. 6C** and **D**) in DOXO + AP–treated mice (gray symbols, surface = 0.041 ± 0.004 and number = 3.39 ± 0.46) relative to those administered doxorubicin alone (purple, symbols, surface = 0.07 ± 0.01 and number = 5.06 ± 0.47). To quantify osteoblast mineralization activity, mice were administered calcein and alizarin 7 days apart and bone formation was assessed at endpoint (**Fig. 6E**). Analyses of the femurs from mice treated with doxorubicin alone (purple symbols) revealed a BFR/BS and a MAR of 0.42 ± 0.06 and 0.86 ± 0.08, respectively (**Fig. 6F** and **G**). Elimination of senescent cells in doxorubicin-treated mice by treating with AP20187 (gray symbols) increased the BFR/BS to 0.87 ± 0.15 and MAR to 1.06 ± 0.10. These data show that chemotherapy-induced senescence drives bone loss by increasing osteoclast activity while simultaneously decreasing osteoblast activity. This agrees with our previous work demonstrating that senescent osteoblasts fail to mineralize bone and increase osteoclastogenesis (49).

Senescent cells express a wide array of factors collectively referred to as SASP factors that have wide-ranging effects on tissue homeostasis (50). We have shown that the p38MAPK-MK2 pathway regulates the expression of many SASP factors (18) and, in the setting of bone metastasis–specific inhibitors of these kinases, preserves bone density (51). Given our findings here that chemotherapy was sufficient to induce senescence, we next asked whether the p38MAPK-MK2 pathway was activated in the bones of treated mice. Indeed, we found that the p38MAPK pathway was activated in the bone following chemotherapy as indicated by the increased appearance of phosphorylated MK2 (**Fig. 7A**). Thus, we next asked whether targeting SASP factors would protect against chemotherapy-induced bone loss. To address this, we administered a p38MAPK inhibitor (p38i) or MAPKAPK2 pathway inhibitor (MK2Pi) *ad libitum* (compounded into chow) to mice treated with four weekly doxorubicin doses (5 mg/kg) and assessed bone density by μCT (**Fig. 7B**). These analyses revealed that the inhibitors had only minimal effects on estrogen levels as assessed by uterine weight (Supplementary Fig. S11A and S11B) but both p38i and MK2Pi treatment reduced SASP factors (**Fig. 7C**) and mitigated chemotherapy-induced bone loss (**Fig. 7D** and **E**). Indeed, we found that the inhibitors had no effect on trabecular bone volume compared with vehicle-treated controls, while doxorubicin treatment induced bone loss (−66.97%) as expected. Strikingly, mice that were administered p38i or MK2Pi in combination with doxorubicin had attenuated trabecular bone loss compared with mice receiving doxorubicin alone (**Fig. 7D** and **E**). The DOXO+p38i–treated group increased trabecular bone volume by 103.21%, while the bone in the DOXO+MK2Pi–treated group increased by 69.89%, relative to the doxorubicin only group (**Fig. 7D** and **E**). Interestingly, the protective effect seemed restricted to the trabecular compartment because we failed to observe significant differences between the doxorubicin-treated and DOXO+p38i or +MK2Pi treatment groups in the cortical compartment (Supplementary Fig. S11C and S11D). Together, these data suggest p38MAPK or MK2 inhibition are viable therapeutic strategies to protect against chemotherapy-induced bone loss.

Discussion

Chemotherapy-induced bone loss has been attributed to estrogen deficiency resulting from ovarian failure (13, 17). Although several clinical studies have hinted that other mechanisms impact bone loss, they have remained largely unexplored. Our results challenge the view that chemotherapy-induced bone loss is primarily estrogen driven and demonstrate that senescence significantly contributes to chemotherapy-induced bone loss independent of estrogen. Furthermore, our findings that inhibition of p38MAPK or MK2, which target the SASP,

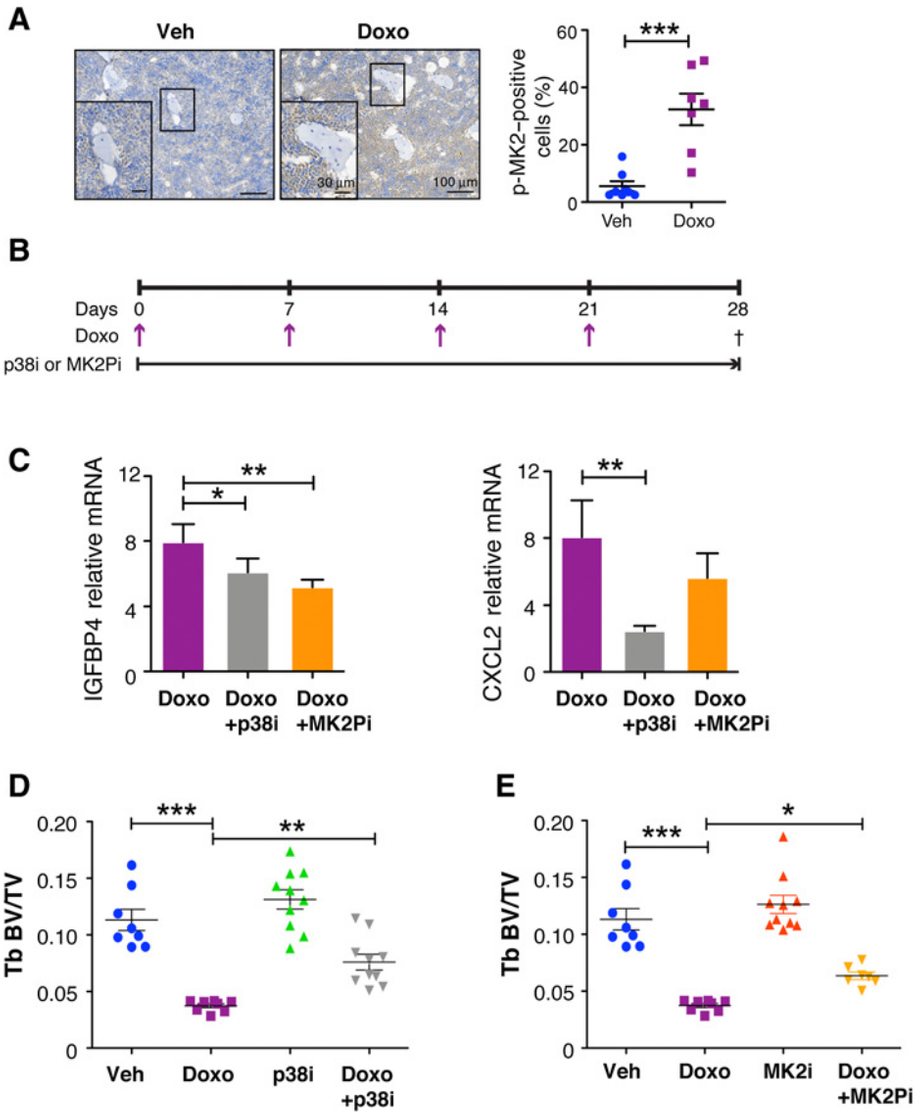

Figure 7.

Inhibition of the p38MAPK-MK2 pathway limits SASP production and rescues chemotherapy-induced bone loss. **A,** Mice were sacrificed on day 28 and bone sections from vehicle and chemotherapy-treated mice were stained for phosphorylated-MK2 . Brown staining shows activation of the p38-MAPK pathway following chemotherapy treatment. $N \geq 7$ per group. Data are presented as mean ± SEM. **B,** Sixteen-week-old C57BL/6 mice were treated with four once weekly doses of vehicle (Veh) or doxorubicin (Doxo; 5 mg/kg) and provided *ad libitum* chow compounded with CDD-111 (p38i) or CDD-450 (MK2Pi). **C,** Mice were sacrificed on day 28 and bone resident cells were isolated from tibias and the SASP factors *Igfbb4* and *Cxcl12* were measured by qRT-PCR. qRT-PCR data are presented as mean ± SD. **D** and **E,** Femurs were isolated from animals treated with vehicle or doxorubicin +/− p38i or +/− MK2Pi and measured by μCT to ascertain bone volume (BV) to trabecular (Tb) volume (BV/TV) of the p38i treatment cohort (**D**). Tb BV/TV of the MK2Pi treatment cohort (**E**). $N \geq 8$ per group. All data are presented as mean ± SEM. *, $P \leq 0.05$; **, $P \leq 0.01$; ***, $P \leq 0.001$.

rescues chemotherapy-induced bone loss suggest that they are viable therapeutic targets that could benefit any patient treated with chemotherapy.

Bone loss is associated with an increased risk of fracture that significantly impacts a survivor's quality of life. Currently, the available treatment options for patients suffering from chemotherapy-induced bone loss are bisphosphonates, denosumab, or hormone replacement (52), which can limit osteoclast differentiation and activity (53, 54). Unfortunately, estrogen and bisphosphonates are not without sequelae. Indeed, bisphosphonates can persist in the skeleton for long periods of time and can result in long-term complications including osteonecrosis of the jaw, hypocalcemia, and kidney toxicity (53, 55). Denosumab use can result in musculoskeletal pain, hypercholesterolemia, and cystitis and its discontinuation has been associated with a rapid decrease in bone density and increased vertebral fracture risk (56). Furthermore, because osteoclast and osteoblast functions are tightly coupled, by killing osteoclasts bisphosphonates ultimately limit osteoblast activity, which can negatively impact bone quality. Estrogens, on the other hand, are not used in cancers that respond to hormones, including estrogen receptor–positive breast cancer (∼70% of patients with breast cancer) or ovarian cancer. Given there is an exponential relationship between bone loss and increased fracture risk (6), the extensive bone loss observed in early stage, nonmetastatic patients argues that safe and potent inhibitors of bone loss are needed. Our data demonstrate that targeting senescent cells and their downstream effector molecules, p38MAPK or MK2 preserves bone in the face of chemotherapy. These data combined with our recent findings that inhibiting p38MAPK and MK2 can significantly reduce metastatic breast cancer growth (51) further suggests that in the metastatic cancer setting, inhibition of these key signaling pathways will have added benefit for patients treated with chemotherapy.

Disclosure of Potential Conflicts of Interest

S.A. Stewart reports receiving a commercial research grant from Aclaris. J. Monahan is an executive vice president R&D (paid consultant) at Aclaris Therapeutics, Inc. D. Baker holds ownership interest (including patents) in Unity Biotechnology. No potential conflicts of interest were disclosed by the other authors.

Disclaimer

Opinions, interpretations, conclusions, and recommendations are those of the authors and are not necessarily endorsed by the Department of Defense. This publication is solely the responsibility of the authors and does not necessarily represent the official view of National Center for Research Resources or the NIH.

Authors' Contributions

Conception and design: Z. Yao, B. Murali, R. Faccio, S.A. Stewart
Development of methodology: Z. Yao, B. Murali, X. Luo, J.M. van Deursen, D. Baker, J.K. Schwarz
Acquisition of data (provided animals, acquired and managed patients, provided facilities, etc.): Z. Yao, B. Murali, J. Monahan, J.M. van Deursen, D. Baker, J.K. Schwarz, S.A. Stewart
Analysis and interpretation of data (e.g., statistical analysis, biostatistics, computational analysis): Z. Yao, S.A. Stewart
Writing, review, and/or revision of the manuscript: Z. Yao, B. Murali, D. Thotala, J. Monahan, D. Baker, J.K. Schwarz, S.A. Stewart
Administrative, technical, or material support (i.e., reporting or organizing data, constructing databases): B. Murali, X. Luo, D.V. Faget, T. Cole, B. Ricci, D. Thotala, S.A. Stewart
Study supervision: B. Murali
Other (provided technical support and important feedback): Q. Ren

Acknowledgments

This work was supported by the Cancer Biology Pathway Molecular Oncology Training Grant NIH T32CA113275 (to B. Murali), NIH grants R01 CA130919 (to S.A. Stewart), and R01 CA181745 (to J.K. Schwarz), and an American Cancer Society Research Scholar Award (to S.A. Stewart). The U.S. Army Medical Research Acquisition Activity, 820 Chandler Street, Fort Detrick, MD 21702-5014, is the awarding and administrating acquisition office, and this was supported in part by the Office of the Assistant Secretary of Defense for Health Affairs, through the Breast Cancer Research Program, under award No. W81XWH-16-1-0728. This work was also supported by the Siteman Cancer Center Investment Program (NCI Cancer Center Support Grant P30CA091842, Fashion Footwear Association of New York, and the Foundation for Barnes-Jewish Hospital Cancer Frontier Fund to S.A. Stewart), a Siteman Cancer Center grant to R. Faccio, NIH grants R01 AR053628 and R01 AR066551 to R. Faccio, and Shriners Hospital grant 85100 to R. Faccio, and J.K. Schwarz is supported by R01 CA181745. Finally, the Glenn Foundation for Medical Research (to J.M. van Deursen and D. Baker) and the NIH (AG057493 to J.M. van Deursen and AG053229 to D. Baker) also supported this work. We thank Deborah Veis and Matthew Silva for their valuable suggestions. We thank Crystal Idleburg and Samantha Coleman at the Musculoskeletal Histology core for their expert technical assistance with bone tissue sectioning and staining. In addition, we thank Daniel Leib, Yung Kim, and Michael Brodt in the Structure and Strength Musculoskeletal core for μCT imaging; Washington University Musculoskeletal Research Center (NIH P30 AR074992). Finally, we thank Lorry Blath and Judy Johnson for their constant support, enthusiasm, and critical assessment of our work and its impact on patients with breast cancer. Imaging and analysis of bone biopsy slides were performed using Zeiss Axio ScanZ.1 at the Washington University Center for Cellular Imaging, which is supported by Washington University School of Medicine, The Children's Discovery Institute of Washington University and St. Louis Children's Hospital (CDI-CORE-2015-505), and the National Institute for Neurological Disorders and Stroke (NS086741). The Centers are partially supported by NCI Cancer Center Support Grant #P30 CA91842 to the Siteman Cancer Center. Finally, we thank Melissa Stauffer of Scientific Editing Solutions for editing the article.

The costs of publication of this article were defrayed in part by the payment of page charges. This article must therefore be hereby marked *advertisement* in accordance with 18 U.S.C. Section 1734 solely to indicate this fact.

Received July 29, 2019; revised November 14, 2019; accepted December 23, 2019; published first January 13, 2020.

References

1. Chao C, Studts JL, Abell T, Hadley T, Roetzer L, Dineen S, et al. Adjuvant chemotherapy for breast cancer: how presentation of recurrence risk influences decision-making. J Clin Oncol 2003;21:4299–305
2. Ishitobi M, Komoike Y, Motomura K, Koyama H, Inaji H. Early response to neoadjuvant chemotherapy in carcinoma of the breast predicts both successful breast-conserving surgery and decreased risk of ipsilateral breast tumor recurrence. Breast J 2010;16:9–13
3. Jones SE, Erban J, Overmoyer B, Budd GT, Hutchins L, Lower E, et al. Randomized phase III study of docetaxel compared with paclitaxel in metastatic breast cancer. J Clin Oncol 2005;23:5542–51
4. Earl H, Provenzano E, Abraham J, Dunn J, Vallier AL, Gounaris I, et al. Neoadjuvant trials in early breast cancer: pathological response at surgery and correlation to longer term outcomes - what does it all mean? BMC Med 2015;13:234
5. Bruning PF, Pit MJ, de Jong-Bakker M, van den Ende A, Hart A, van Enk A. Bone mineral density after adjuvant chemotherapy for premenopausal breast cancer. Br J Cancer 1990;61:308–10
6. Guise TA.Bone loss and fracture risk associated with cancer therapy. Oncologist 2006;11:1121–31
7. Falahati-Nini A, Riggs BL, Atkinson EJ, O'Fallon WM, Eastell R, Khosla S. Relative contributions of testosterone and estrogen in regulating bone resorption and formation in normal elderly men. J Clin Invest 2000;106:1553–60
8. Duursma SA, Raymakers JA, Boereboom FT, Scheven BA. Estrogen and bone metabolism. Obstet Gynecol Surv 1992;47:38–44
9. Khosla S.Pathogenesis of age-related bone loss in humans. J Gerontol A Biol Sci Med Sci 2013;68:1226–35
10. Blume SW, Curtis JR.Medical costs of osteoporosis in the elderly Medicare population. Osteoporos Int 2011;22:1835–44
11. Khalid AB, Krum SA. Estrogen receptors alpha and beta in bone. Bone 2016;87:130–5
12. Cenci S, Weitzmann MN, Roggia C, Namba N, Novack D, Pacifici R. Estrogen deficiency induces bone loss by enhancing T cell production of TNF-alpha. J Clin Invest 2000;106:1229–37
13. Cameron DA, Douglas S, Brown JE, Anderson RA. Bone mineral density loss during adjuvant chemotherapy in pre-menopausal women with early breast cancer: is it dependent on oestrogen deficiency? Breast Cancer Res Treat 2010;123:805–14
14. Saad F.New research findings on zoledronic acid: survival, pain, and anti-tumour effects. Cancer Treat Rev 2008;34:183–92
15. Greep NC, Giuliano AE, Hansen NM, Taketani T, Wang HJ, Singer FR. The effects of adjuvant chemotherapy on bone density in postmenopausal women with early breast cancer. Am J Med 2003;114:653–9
16. Rodriguez-Rodriguez LM, Rodriguez-Rodriguez EM, Oramas-Rodriguez JM, Santolaria-Fernandez F, Llanos M, Cruz J, et al. Changes on bone mineral density after adjuvant treatment in women with non-metastatic breast cancer. Breast Cancer Res Treat 2005;93:75–83
17. Shapiro CL, Manola J, Leboff M. Ovarian failure after adjuvant chemotherapy is associated with rapid bone loss in women with early-stage breast cancer. J Clin Oncol 2001;19:3306–11
18. Alspach E, Flanagan KC, Luo X, Ruhland MK, Huang H, Pazolli E, et al. p38MAPK plays a crucial role in stromal mediated tumorigenesis. Cancer Discov 2014;4:716–29
19. Woods D, Turchi JJ. Chemotherapy induced DNA damage response: convergence of drugs and pathways. Cancer Biol Ther 2013;14:379–89
20. Selvarajah J, Nathawat K, Moumen A, Ashcroft M, Carroll VA. Chemotherapy-mediated p53-dependent DNA damage response in clear cell renal cell carcinoma: role of the mTORC1/2 and hypoxia-inducible factor pathways. Cell Death Dis 2013;4:e865
21. Demaria M, O'Leary MN, Chang J, Shao L, Liu S, Alimirah F, et al. Cellular senescence promotes adverse effects of chemotherapy and cancer relapse. Cancer Discov 2017;7:165–76
22. Sun M, Li WW, Yu HQ, Harada H. A novel integrated approach to quantitatively evaluate the efficiency of extracellular polymeric substances (EPS) extraction process. Appl Microbiol Biotechnol 2012;96:1577–85
23. Wood JG, Jones BC, Jiang N, Chang C, Hosier S, Wickremesinghe P, et al. Chromatin-modifying genetic interventions suppress age-associated transposable element activation and extend life span in Drosophila. Proc Natl Acad Sci U S A 2016;113:11277–82
24. Campisi J, Kim SH, Lim CS, Rubio M. Cellular senescence, cancer and aging: the telomere connection. Exp Gerontol 2001;36:1619–37

25. Farr JN, Xu M, Weivoda MM, Monroe DG, Fraser DG, Onken JL, et al. Targeting cellular senescence prevents age-related bone loss in mice. Nat Med 2017;23: 1072–9
26. Sledge GW, Neuberg D, Bernardo P, Ingle JN, Martino S, Rowinsky EK, et al. Phase III trial of doxorubicin, paclitaxel, and the combination of doxorubicin and paclitaxel as front-line chemotherapy for metastatic breast cancer: an intergroup trial (E1193). J Clin Oncol 2003;21:588–92
27. Nagar S.Pharmacokinetics of anti-cancer drugs used in breast cancer chemotherapy. Adv Exp Med Biol 2010;678:124–32
28. Hadji P, Ziller M, Maskow C, Albert U, Kalder M. The influence of chemotherapy on bone mineral density, quantitative ultrasonometry and bone turnover in premenopausal women with breast cancer. Eur J Cancer 2009;45:3205–12
29. Shusterman S, Meadows AT.Long term survivors of childhood leukemia. Curr Opin Hematol 2000;7:217–22
30. Farr J, Rowsey J, Eckhardt B, Thicke B, Fraser D, Tchkonia T, et al. Independent roles of estrogen deficiency and cellular senescence in the pathogenesis of osteoporosis: evidence in young adult mice and older humans. J Bone Miner Res 2019:34:1407–18
31. Ottewell PD, Deux B, Monkkonen H, Cross S, Coleman RE, Clezardin P, et al. Differential effect of doxorubicin and zoledronic acid on intraosseous versus extraosseous breast tumor growth in vivo. Clin Cancer Res 2008;14:4658–66
32. Rana T, Chakrabarti A, Freeman M, Biswas S. Doxorubicin-mediated bone loss in breast cancer bone metastases is driven by an interplay between oxidative stress and induction of TGFbeta. PLoS One 2013;8:e78043
33. Haffner-Luntzer M, Kovtun A, Lackner I, Modinger Y, Hacker S, Liedert A, et al. Estrogen receptor alpha- (ERα), but not ERβ-signaling, is crucially involved in mechanostimulation of bone fracture healing by whole-body vibration. Bone 2018;110:11–20
34. Amin S, Zhang Y, Sawin CT, Evans SR, Hannan MT, Kiel DP, et al. Association of hypogonadism and estradiol levels with bone mineral density in elderly men from the framingham study. Ann Intern Med 2000;133:951–63
35. Szulc P, Garnero P, Munoz F, Marchand F, Delmas PD. Cross-sectional evaluation of bone metabolism in men. J Bone Miner Res 2001;16:1642–50
36. Khosla S, Riggs BL, Atkinson EJ, Oberg AL, Mavilia C, Del Monte F, et al. Relationship of estrogen receptor genotypes to bone mineral density and to rates of bone loss in men. J Clin Endocrinol Metab 2004;89:1808–16
37. Khosla S. Estrogen and bone: insights from estrogen-resistant, aromatase-deficient, and normal men. Bone 2008;43:414–7
38. Ongphiphadhanakul B, Piaseu N, Chailurkit L, Rajatanavin R. Suppression of bone resorption in early postmenopausal women by intranasal salmon calcitonin in relation to dosage and basal bone turnover. Calcif Tissue Int 1998;62:379–82
39. Chandra A, Lin T, Young T, Tong W, Ma X, Tseng WJ, et al. Suppression of sclerostin alleviates radiation-induced bone loss by protecting bone-forming cells and their progenitors through distinct mechanisms. J Bone Miner Res 2017; 32:360–72
40. Jia D, Gaddy D, Suva LJ, Corry PM. Rapid loss of bone mass and strength in mice after abdominal irradiation. Radiat Res 2011;176:624–35
41. Wright LE, Buijs JT, Kim HS, Coats LE, Scheidler AM, John SK, et al. Single-limb irradiation induces local and systemic bone loss in a murine model. J Bone Miner Res 2015;30:1268–79
42. Campisi J, d'Adda di Fagagna F. Cellular senescence: when bad things happen to good cells. Nat Rev Mol Cell Biol 2007;8:729–40
43. Dimri GP, Lee X, Basile G, Acosta M, Scott G, Roskelley C, et al. A biomarker that identifies senescent human cells in culture and in aging skin *in vivo*. Proc Natl Acad Sci U S A 1995;92:9363–7
44. Lee SK, Gardner AE, Kalinowski JF, Jastrzebski SL, Lorenzo JA. RANKL-stimulated osteoclast-like cell formation *in vitro* is partially dependent on endogenous interleukin-1 production. Bone 2006;38:678–85
45. Bouxsein ML, Myers KS, Shultz KL, Donahue LR, Rosen CJ, Beamer WG. Ovariectomy-induced bone loss varies among inbred strains of mice. J Bone Miner Res 2005;20:1085–92
46. Streicher C, Heyny A, Andrukhova O, Haigl B, Slavic S, Schuler C, et al. Estrogen regulates bone turnover by targeting RANKL expression in bone lining cells. Sci Rep 2017;7:6460
47. Baker DJ, Wijshake T, Tchkonia T, LeBrasseur NK, Childs BG, van de Sluis B, et al. Clearance of p16Ink4a-positive senescent cells delays ageing-associated disorders. Nature 2011;479:232–6
48. Baker DJ, Dawlaty MM, Wijshake T, Jeganathan KB, Malureanu L, van Ree JH, et al. Increased expression of BubR1 protects against aneuploidy and cancer and extends healthy lifespan. Nat Cell Biol 2013;15:96–102
49. Luo X, Fu Y, Loza AJ, Murali B, Leahy KM, Ruhland MK, et al. Stromal-initiated changes in the bone promote metastatic niche development. Cell Rep 2016;14: 82–92
50. Rodier F, Campisi J.Four faces of cellular senescence. J Cell Biol 2011;192:547–56
51. Murali B, Ren Q, Luo X, Faget DV, Wang C, Johnson RM, et al. Inhibition of the stromal p38MAPK/MK2 pathway limits breast cancer metastases and chemotherapy-induced bone loss. Cancer Res 2018;78:5618–30
52. Stopeck AT, Lipton A, Body JJ, Steger GG, Tonkin K, de Boer RH, et al. Denosumab compared with zoledronic acid for the treatment of bone metastases in patients with advanced breast cancer: a randomized, double-blind study. J Clin Oncol 2010;28:5132–9
53. Coleman RE, Major P, Lipton A, Brown JE, Lee KA, Smith M, et al. Predictive value of bone resorption and formation markers in cancer patients with bone metastases receiving the bisphosphonate zoledronic acid. J Clin Oncol 2005;23: 4925–35
54. Michaud LB.Managing cancer treatment-induced bone loss and osteoporosis in patients with breast or prostate cancer. Am J Health Syst Pharm 2010;67: S20–30.
55. Khosla S, Burr D, Cauley J, Dempster DW, Ebeling PR, Felsenberg D, et al. Bisphosphonate-associated osteonecrosis of the jaw: report of a Task Force of the American Society for bone and mineral research. J Bone Miner Res 2007;22: 1479–91
56. Lewiecki EM.New and emerging concepts in the use of denosumab for the treatment of osteoporosis. Ther Adv Musculoskelet Dis 2018;10:209–23